ACS APPLIED MATERIALS & INTERFACES

RESEARCH ARTICLE

www.acsami.org

Controlled Effect of Ultrasonic Cavitation on Hydrophobic/Hydrophilic Surfaces

Valentina Belova,*[,†] Dmitry A. Gorin,[†,‡] Dmitry G. Shchukin,[†] and Helmuth Möhwald[†]

[†]Department of Interfaces, Max-Planck Institute of Colloids and Interfaces, Potsdam, D14476, Germany

[‡]Faculty of Nano- and Biomedical Technologies, Saratov State University, Saratov, 410012, Russia

ABSTRACT: Controlling cavitation at the solid surface is of increasing interest, as it plays a major role in many physical and chemical processes related to the modification of solid surfaces and formation of multicomponent nanoparticles. Here, we show a selective control of ultrasonic cavitation on metal surfaces with different hydrophobicity. By applying a microcontact printing technique we successfully formed hydrophobic/hydrophilic alternating well-defined microstructures on aluminium surfaces. Fabrication of patterned surfaces provides the unique opportunity to verify a model of heterogeneous nucleation of cavitation bubbles near the solid/water interface by varying the wettability of the surface, temperature and ultrasonic power. At the initial stage of sonication (up to 30 min), microjets and shock waves resulting from the collapsing bubbles preferably impact the hydrophobic surface, whereas the hydrophilic areas of the patterned Al remain unchanged. Longer sonication periods affect both surfaces. These findings confirm the expectation that higher contact angle causes a lower energy barrier, thus cavitation dominates at the hydrophobic surfaces. Experimental results are in good agreement with expectations from nucleation theory. This paper illustrates a new approach to ultrasound induced modification of solid surfaces resulting in the formation of foam-structured metal surfaces.

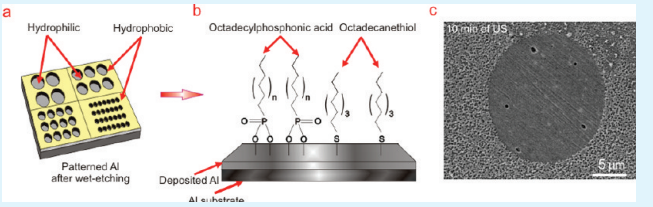

KEYWORDS: heterogeneous nucleation, ultrasound, cavitation, aluminium, hydrophobic and hydrophilic surface, nucleation energy, nucleation rate

INTRODUCTION

Heterogeneous bubble nucleation at the solid surface under ultrasonic irradiation has become an important issue in sonochemistry.[1,4] Prediction and control of the effect of the cavitation collapse on different surfaces are extremely complex problems because the bubbles can translate, grow, and interact with each other. The extreme pressure and temperature generated by shock waves and liquid jets can damage the surface locally forming various surface structures.[5,6] These phenomena occur in a short time interval (less than millisecond).[7,8] Although ultrasonic irradiation is intensively applied in nanocomposite production,[9−12] as a catalyst in chemical synthesis[13−15] and for special pre-treatment of solid surfaces,[16−18] the mechanism of ultrasonic-action on the solid surfaces is still poorly understood. One major goal of sonochemistry is to quantitatively understand and control the formation of cavitation bubbles at solid surfaces and to understand the influence of the collapsing bubbles on the surfaces. Controlling the nucleation process may lead to new applications of ultrasonic irradiation to fabricate novel materials with defined physical/chemical properties. This can open a new perspective for sonochemistry to be effectively integrated in surface chemistry. Generally, there have been two recent developments providing new routes for studies of cavitation at surfaces: high-speed cameras enabled observations of the time development of bubble shapes and microstructuring of the surfaces enabled control of the contact of a bubble with a surface.

The latter topic is a central theme of this work where the surface is endowed a lateral chemical contrast with micrometer dimensions.

To present, two types of factors strongly influence gas bubble nucleation at the solid surface under sonication: (1) the conditions of sonication (temperature of the solution,[19] surfactants,[20] presence of particles,[21,22] gas phase[23]) and (2) the properties of the solid surface (roughness (24), wettability[25]). Control of the surface energy can be achieved by using specific substrates or by coating a substrate with suitable polymers or surfactants.[18,21] In the 1970s, Nail et al. studied unpolished stainless steel boiled surfaces and reported cavities and grooves as active sites for nucleation.[26] Nucleation on a solid surface is mostly caused by irregularities, such as grain boundaries, edges, cracks, and scratches on the surface. According to work of Bremond et al. (2006), the gas bubbles prefer a hydrophobic surface. The authors carried out multibubble surface-cavitation experiments by using a hydrophobic surface patterned with microcavities.[27,28] The authors found that the expansion of the nuclei in the microcavities is triggered by a fast lowering of the liquid pressure. This process allows controlling and fixing the bubble distance within the bubble cluster. Harvey's research group suggested that the crevices attaching the nuclei should also have a hydrophobic

Received: October 18, 2010
Accepted: December 31, 2010
Published: January 31, 2011

Scheme 1. (a) Nucleation and growth of a cavitation bubble at a surface. The pressure P' performing the volume work is given by the vapour pressure P_V of the liquid; the gas pressure P_G and the acoustic pressure P_A being in excess of the external pressure P_L (see text). (b) Dependence of the volume work (E_b), the surface energy (E_s) and superposition result ($E_s + E_b$) on the radius of a gas bubble. (c) Nucleation energy barrier as a function of contact angle θ. The center regions marked by the vertical lines correspond to the contact angles applied in this work

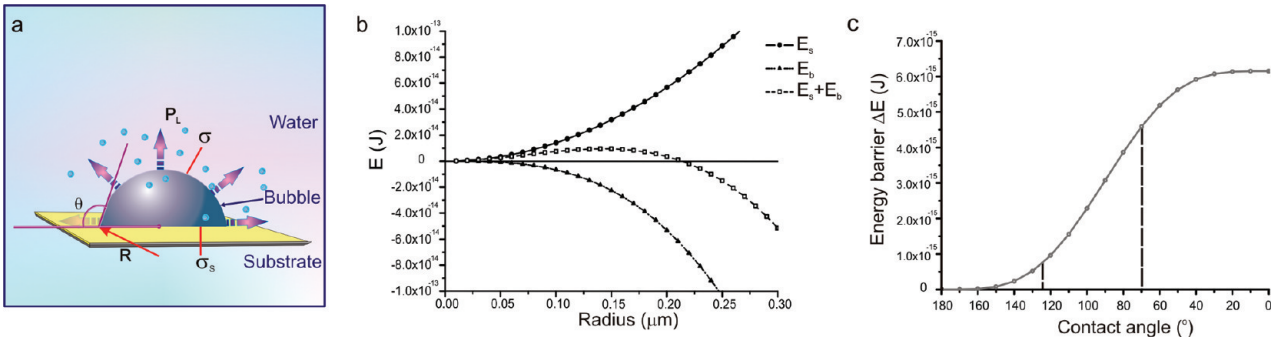

surface.[29] Additionally, we refer to Lohse et al., who studied the acoustic nucleation threshold for bubbles, by applying a single pressure pulse to bubbles trapped in cylindrical nanoscopic pits ("artificial crevices").[30] Upon immersion in water, the hydrophobic nanopits trapped air and served as nucleation sites. Another very important finding by Neutron reflectometry is that the water density near a hydrophobic surface is reduced.[31] Also studies of nanobubbles (the residual gas) in liquid prove that they are preferentially located at the hydrophobic surface.[32]

The actions of ultrasound result from chemical reaction due to the production of radicals at the high temperatures as well as physical ones. The latter are on the one hand due to shock waves that form upon radial collapse of a bubble. On the other hand, the symmetry break near an interface may cause a jet, a fluid flow into the center of the bubble and towards the surface. A way to study surface cavitation is to examine nucleation phenomena, which can be strongly affected by presence of both hydrophobic and hydrophilic phases. In a recent investigation,[33] we briefly introduced a new effective solution for controlling the heterogeneous nucleation process at solid surfaces based on microcontact printing resulting in well-defined hydrophobic/hydrophilic microstructures on a solid substrate. It has been also possible to develop a set of equations that explain the experimental findings. This study has shed new light onto the mechanism of ultrasound-induced nucleation on bulk hydrophobic/hydrophilic surfaces.

In the present paper, we provide more insight into the mechanisms by a more detailed analysis of the corresponding steps: in the theoretical background we will describe our model of heterogeneous bubble nucleation at the solid surface under sonication. We will then illustrate the microcontact printing technique for fabrication of the hydrophobic/hydrophilic aluminium surfaces and analyse structures in detail. The changes of the patterned surfaces during sonication are illustrated with the following analytical techniques: scanning electron microscopy (SEM), Fourier transform infrared measurements (FTIR), atomic force microscopy (AFM), and contact angle (CA) measurements.

THEORETICAL BACKGROUND

The bubble formation on a liquid/solid interface is given in Scheme 1a. The surface energy E_S, the energy of the liquid/gas and solid/gas interface of the bubble, is related to the contact angle θ by

$$E_S = \pi R^2 \sigma g(\theta) \tag{1}$$

with R being the curvature radius of the droplet, σ the liquid/air surface tension, and $g(\theta) = 2+3\cos\theta - \cos^3\theta$ being a function monotonously decaying with increasing θ.[34] The surface energy of a bubble in the bulk is obtained for $\theta = 0°$. For a bubble to be formed, a pressure P has to perform work on the gas with volume V_b. Thus the pressure P, the difference from the outside hydrostatic pressure of the liquid, results from possible entrapped gas with partial pressure P_G, vaporized liquid with partial pressure P_V,[35] the largest contribution being the acoustic pressure upon rarefaction P_A:[36]

$$P = P_A + P_G + P_V \tag{2}$$

The corresponding work is then

$$E_b = -\frac{\pi}{3} R^3 g(\theta) P \tag{3}$$

If we insert as P_A, the maximum pressure we thus calculate the minimum energy barrier for nucleation. So, we basically assume that bubble nucleation occurs at the maximum of the rarefaction amplitude. The dependences of the two opposing energies with different powers of R cause a typical nucleation scenario (see Scheme 1b) where growth continues beyond a critical radius R_c defined by

$$\frac{d(E_s + E_b)}{dR}(R_c) = 0 \tag{4}$$

and the corresponding energy barrier is derived as

$$(E_s + E_b)(R_c) = \Delta E = \frac{4\pi}{3}\frac{\sigma^3}{P^2} g(\theta) \tag{5}$$

If nucleation results from thermal activation across the barrier E_b, the bubble nucleation rate dN/dt given by

$$J = \frac{dN}{dt} = \text{constant}\left(\exp\left(-\frac{\Delta E}{kT}\right)\right) \tag{6}$$

In the experiments below, we vary the contact angle θ, the temperature T, and the acoustic pressure P_A with results qualitatively as expected from eq 6, as will be demonstrated.

Scheme 2. Sketch of a Pattern and the Molecules (ODPA and ODT) Used for Hydrophobization of the Aluminium Surface by Microcontact Printing

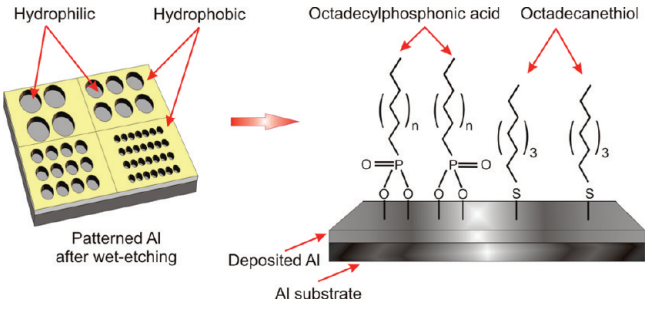

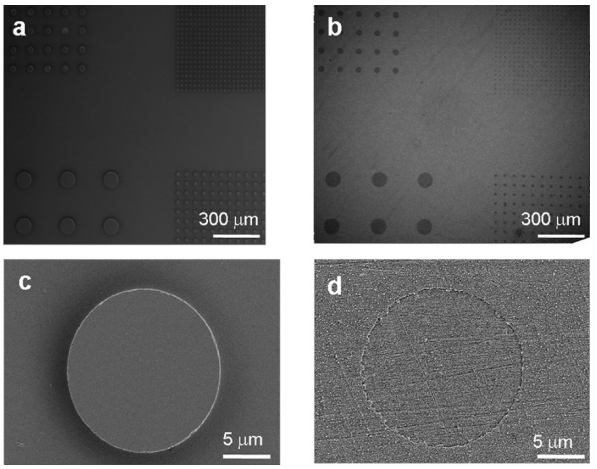

Figure 1. ESEM and SEM images of the Si-Master (a, c) and patterned Al plate (b, d), where the inner circular area is hydrophilic, the outer part is hydrophobic.

RESULTS AND DISCUSSION

We investigated gas bubble nucleation on a hydrophobic/hydrophilic microstructure. Details concerning the microstructure are given in the Experimental Section. Polydimethylsiloxane has been used to transfer a mixture of octadecylphosphonic acid (ODTA) and octadecanethiol (ODT) to the Al surface where they form a self-assembled monolayer (SAM) with approximate thickness of 3 nm, which is congruent with the surface relief pattern of the stamp (Scheme 2). We obtained patterned Al samples with precisely defined shapes, location and contact line boundaries (Figure 1b, d). The pattern has four fields of lateral hydrophobic surfaces with regular cylindrical hydrophilic areas with a contact angle (measured separately) of 70° where the amphiphilic ODTA and ODT have not been adsorbed on the Al surface by stamping. They exhibit only a small area fraction, hence the macroscopically measured angle essentially corresponds to that of the hydrophobic area with contact angle in the range of 114° - 125° (Table 1). This design allows us to investigate the changes in the surface energy of a patterned Al plate under ultrasonic irradiation.

The infrared reflection absorption (IRRA) spectrum of the patterned Al shows the phosphonate group P−O at 1267 cm^{-1} and P═O at 1160 cm^{-1} corresponding to the functional groups of ODPA and ODT (Figure 2 top, patterned Al). We observe the conformational order of the ODPA and ODT by studying the

Table 1. Characteristics for the Four Different Fields of the Pattern

Field of the patterned Al	Initial contact angle, θ	Diameter of the hydrophilic holes (μm)	Interspacing (μm)
A1	123.9 ± 0.012	9.0 ± 0.01	34.0 ± 0.01
A2	116.4 ± 0.014	19.2 ± 0.01	67.2 ± 0.01
A3	114.9 ± 0.003	45.2 ± 0.01	140.3 ± 0.01
A4	114.4 ± 0.015	100.0 ± 0.01	300.0 ± 0.01

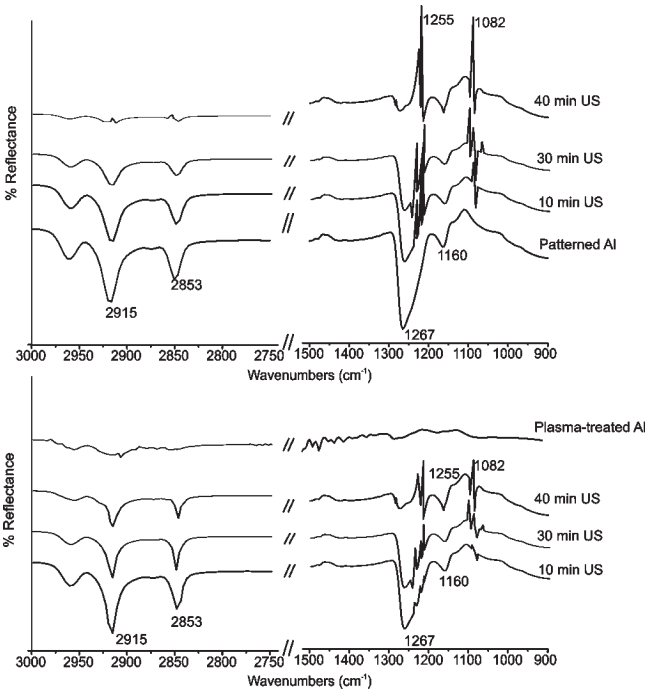

Figure 2. Top: IRRA spectra of the patterned Al surface at different time of sonication (10, 30, and 40 min) at 340 K. Bottom: IRRA spectra of the patterned Al at different time of sonication (10, 30, and 40 min) at 293 K. All spectra were shifted along the transmittance axis for clarity but measured with the same sensitivity.

position of the CH_2 stretching band in the IRRA spectrum. For conformationally ordered systems of crystalline alkanes, the peaks appear at 2915 and 2853 cm^{-1}, corresponding to antisymmetric and symmetric stretch of the CH_2 groups.[37] This observation indicates the formation of SAM on the Al surface. Figure 3a shows well-defined AFM images of the patterned Al substrate (diameter of hydrophilic holes is 19.2 μm, interspacing equal to 67.2 μm) after wet etching. The scan size is 30 μm × 30 μm and the height range is approximately 100 nm. We indeed confirm that patterned Al samples consist of a flat hydrophobic terrace separated by steps of 100 nm with hydrophilic holes.

The experiments were carried out at 20 kHz and power densities of 29, 40, 51.3 W/cm^2 (ultrasonic processor UIP1000 hd from Hielscher Ultrasonics GmbH Teltow, Germany). During all experiments the patterned Al samples were loaded in a home made Teflon sample holder which was fixed parallel to the ultrasonic flat sonotrode (3.14 cm^2 area) at a distance of 15 mm. A labour metal support, placed outside of home manufactured sonoreactor, permitted to fix the sample holder at a different distance between the sonotrode and the sample. The sonoreactor was connected with a cryostat (FRYKA-Kältetechnik GmbH (KT06-42 400 W, Esslingen, Germany) for controlling the tem-

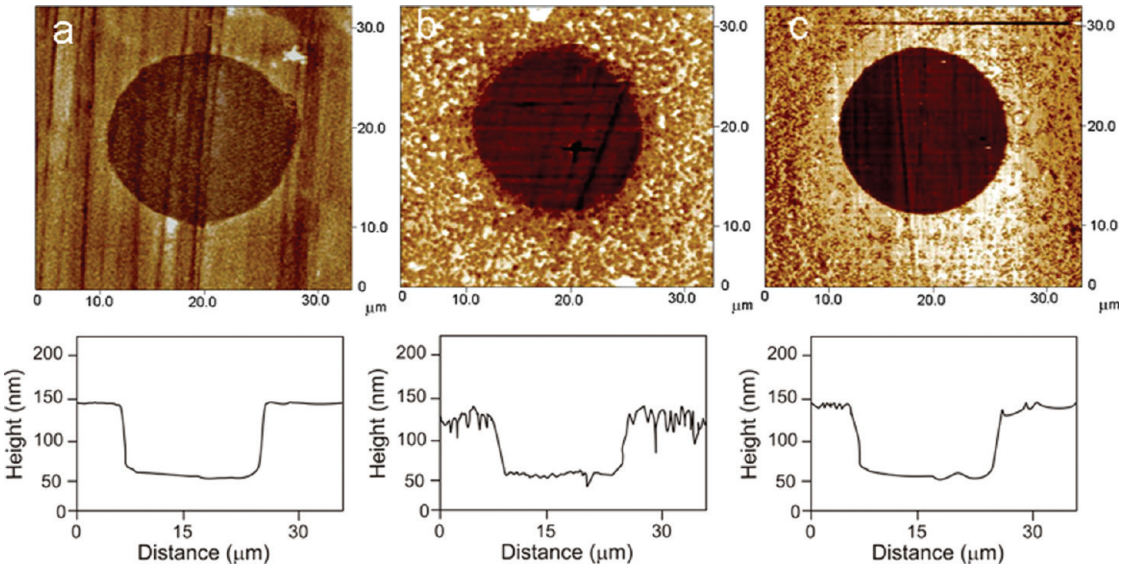

Figure 3. AFM images of the patterned Al plates: (a) initial; (b) −340 K (at 30 min of sonication; (c) −293 K (at 30 min of sonication).

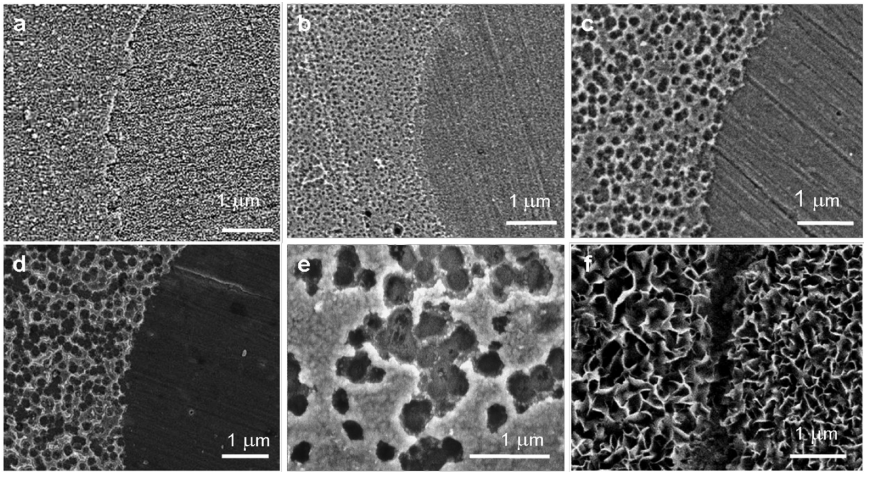

Figure 4. SEM images of the patterned Al plate (a) before ultrasonic treatment and (b−f) after ultrasonic treatment: (b) at 5 min of sonication, (c) at 10 min of sonication, (d) at 30 min of sonication, (e) high magnification of the hydrophobic surface with pits at 30 min of sonication, (f) at 40 min of sonication. Temperature of the treatment is 340 K.

perature of sonicated water (volume was about 200 ml). We compared two situations: (1) samples irradiated at 340 K, (2) samples irradiated at 293 K ± 1 K. For pictorial clarity, the results are henceforth illustrated at 51.3 W/cm^2, because at this power density the effects of the bubble collapse and microjet impact on the surface are strongest.

SEM images of a molded Al plate at various irradiation times (at 340 K) are shown in Figure 4. We observe that the hydrophilic plane of the molded Al (holes) is not affected by cavitation at the earlier stage of the ultrasonic treatment (up to 30 min), whereas the hydrophobic part shows various stages of damaging forming a foam-like metal structure on the surface, which depends on sonication time. When the surface reacts, dark pits appear related to microjet and shock wave impingement after asymmetrical collapse of gas bubbles at the Al surface (Figure 4b). The dimensions of these pits are mostly below 0.5 μm. With increasing sonication time, the pits become more pronounced at t = 30 min (Figure 4c). They have a crater-like shape and are irregularly distributed on the surface. Most of the pits are overlapping each other forming big cavities and, finally, a foamlike structure. Longer sonication periods show dramatic changes in the molded Al surface. Apparently, at later time of ultrasonic treatment nucleation occurs at the planar hydrophilic surface as well. Both hydrophobic and hydrophilic surfaces have a similar microrough structure after 40 min of ultrasonic treatment. However, we notice that a hydrophobic surface is much stronger affected by cavitation than the hydrophilic one (Figure 4f). In addition, after 40 min of sonication, traces of the pattern borders are still present at the surface and seem to be untouched.

The contact angle measurements of the patterned Al samples show a drastic change in surface wettability. We observe changes of the total hydrophobicity of the patterned Al surface towards hydrophilic due to the action of ultrasonic irradiation on the surface. After 60 min of sonication, the CA drops from 124° to 59−70° (depending on the diameter of the hydrophilic holes and interspacing) and these values do not change drastically with further increasing the time of ultrasonic treatment (Figure 5a and Table 1). The IRRA spectra show a significant decrease of the

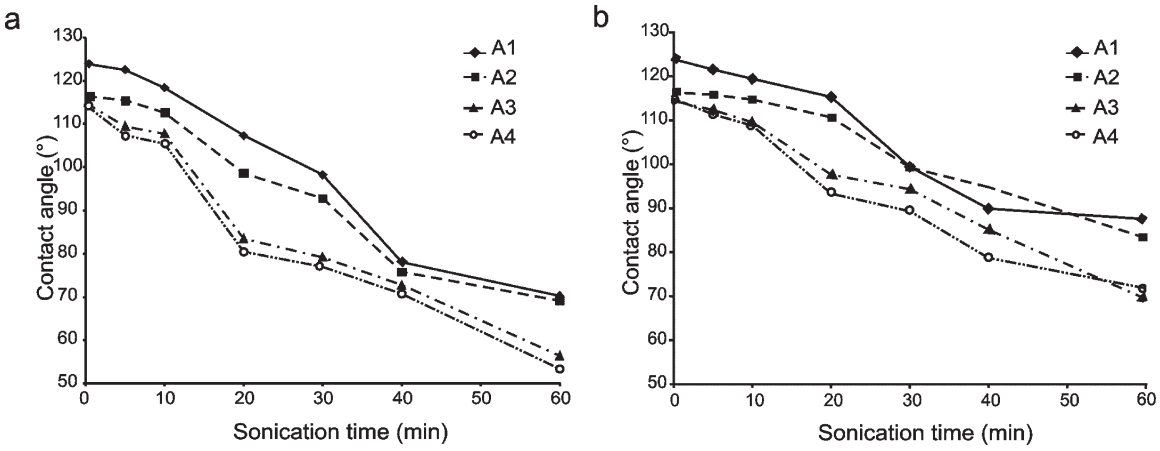

Figure 5. Plot of contact angle versus sonication time for ultrasonic power 51.3 W/cm^2 at (a) 340 and (b) 293 K. The four types of surfaces A1 to A4 correspond to the four different patterns in the figure.

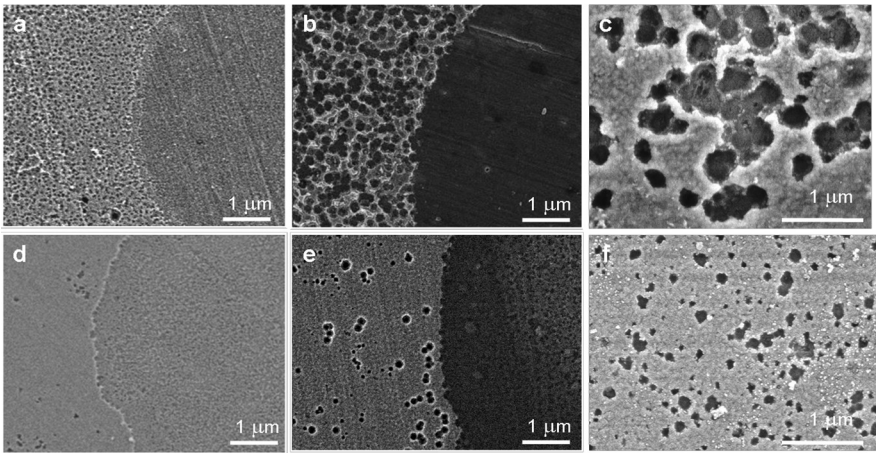

Figure 6. Comparison of SEM images of the patterned Al plates after ultrasonic treatment at 340 K (on the top) and 293 K (on the bottom): (a, d) at 5 min of sonication, (b, e) at 30 min of sonication, (c, f) high magnification of the hydrophobic surface with pits at 30 min of sonication.

absorption peaks corresponding to the phosphonate group P−O at 1050 cm^{-1} and P═O at 1160 cm^{-1}. The anti-symmetric and symmetric CH_2 stretching band intensities (at 2915 and at 2853 cm^{-1}) are decreased with increasing sonication time. After 40 min of ultrasonic irradiation, the peaks completely disappear (Figure 2 Top). At the same time, we notice an increase in the hydroxyl group concentration in the new oxide film. The increased bands at 1082 and 1255 cm^{-1} are attributed to vibrations of the Al−OH bands.[38,39] AFM data given in Figure 4b show the surface of the patterned Al after 30 min of ultrasonic treatment. Similar changes in the surface topography of treated samples are found for all four fields of the patterned Al. As can be seen in Figure 3b, AFM images change dramatically after ultrasonic treatment. After 30 min of ultrasonic irradiation, the height difference between hydrophobic and hydrophilic areas is in average reduced to 80 nm. We note that the defects (pits) are on the order of the radius of curvature of the pyramidal AFM tip. Longer sonication drastically decreases the step between the planar and the upper part of the patterned Al.

Higher temperature is expected to act manifold: (i) it facilitates the overcoming of the nucleation barrier in eq 6, (ii) it increases the vapor pressure P_V and decreases the Laplace pressure via σ and σ itself entering with σ^3 into eq 5, (iii) the surface energy decreases with increasing temperature. These are indeed observed comparing the results at room temperature (293 K) and at 340 K. The pits resulting at higher temperature are apparently also larger merging with each other (compare Figure 6c, f). The fact that pits are observed with micrometer-sized contact on the hydrophobic surfaces indicates that they result from microjets. These would act directly under the center of the bubble whereas a shock wave would create pits concentrically around this center, hence also on the hydrophobic areas. We observe a delay of microjet action on the surfaces in case of ultrasonic treatment at room temperature (Figure 6a, d). Here, at the earlier step of the sonication, the strikes of the microjets are less pronounced. After 30 min of ultrasonic irradiation pits undergo almost no collision in contrast to the situation at T = 340 K at the same time (Figure 6b, e). In addition, the boundaries have almost no "crater" effect. The pits have very flat boundaries with inner grid structure. It leads to compact island shapes avoiding the formation of fractured structures. The comparison of these two conditions suggests that the effect of temperature is one of the major issues in the nucleation process on the solid surface.

The IRRA spectra of the patterned Al (for T = 293 K) at different sonication time are presented in Figure 2 (bottom). Up to 30 min sonication time, we observe a weaker and slower decrease in the 1050 and 1160 cm^{-1} absorption peaks than measured at T = 340 K. Additionally, the absorption peaks of the

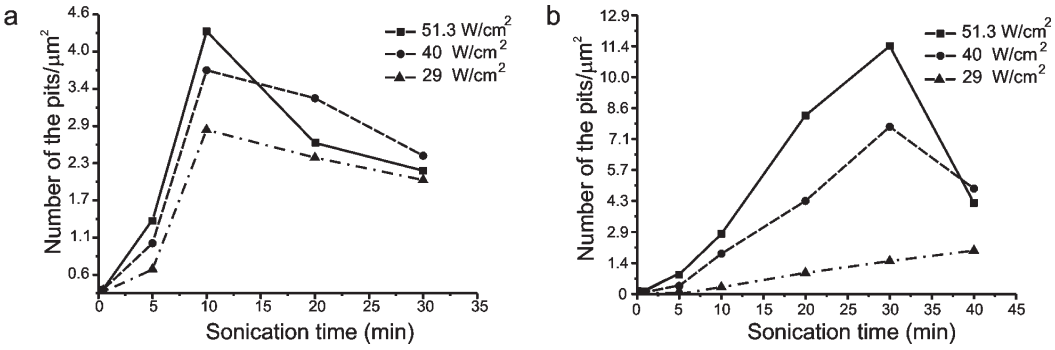

Figure 7. Plot of the pit numbers for different ultrasonic irradiation power as a function of sonication time: (a) 340 and (b) 293 K (diameter of hydrophilic holes is 19.2 μm, interspacing is 67.2 μm).

anti-symmetric and symmetric CH_2 stretching vibrations are slightly decreased. These peaks are significantly reduced after only 40 min of ultrasonic irradiation. This indicates that the SAM is mainly destroyed at the patterned Al surface. Intensities at 1082 and 1255 cm^{-1}, which are attributed to vibration of Al−OH, increase with sonication time. Furthermore, AFM measurements confirm that the roughening of the hydrophobic surface within the first 30 min of sonication is not significant (Figure 3c). The contact angle slightly decreases at the first stage of sonication, which can be interpreted as slowly developing nucleation on the surface (Figure 5b). When the sonication is conducted with cooling of the solution up to 293 K, the rate of pit formation is distinctly lower than at higher temperature. For longer sonication time (> 60 min), the CA changes to 95−80°.

To quantitatively analyze the surface damage, we examined SEM images obtained at various temperatures, sonication times and ultrasonic power by applying the statistical Software Image J. We estimated the number of pits formed by sonication on the reference area ($7 \times 5\ \mu m^2$). Each time, we analyzed three SEM images to find average values. To highlight the inhomogeneous collapse distribution on the surface, we plotted the pit density for different ultrasonic irradiation power as a function of sonication time (Figure 7). One realizes that there is a lag phase, and then a steep increase in the number of pits per time. This lag phase may indicate that initially created nanobubbles assemble on the hydrophobic surface to form the nucleus described via eq 5. Beyond a maximum, there is the merger of pits, which makes quantification meaningless. At this stage, the SAM is strongly affected by the microjets, which make the nucleation process at the surface more chaotic. One clearly observes an increase of the nucleation rate with temperature by a factor of 2 (compare the difference between 5 and 10 minutes) for the temperatures 293 and 340 K and with ultrasonic power (Figure 7b). The changes are most pronounced at 293 K, indicating that the system is near a threshold considering the nucleation rate as a function of ultrasonic intensity. The latter enters via the acoustic pressure P_A, which is varied by only 30 % because of the square root dependence on power. This estimation gives us a first preliminary view on the nucleation process on the hydrophobic surface at the boundary with a hydrophilic surface, which strongly depends on the power and time of ultrasonic irradiation.

Even though we did not determine any threshold for cavitation as might be expected by nucleation theory, we should comment on the importance of different parameters varied here in conjunction with the equation $(\Delta E=(4\pi/3)(\sigma^3/P^2)g(\theta))$. Scheme 1c gives the variation of the energy barrier with θ which

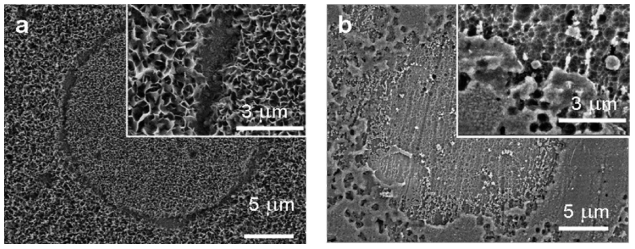

Figure 8. SEM images of the plasma-treated sample (a) after 10 min of sonication and (b) after 10 min of boiling-treatment.

is proportional to the geometrical factor $g(\theta)$. This barrier is reduced by more than a factor of 5 compared to the hydrophilic surface areas (CA = 70°), hence clearly explaining the findings of surface selective impact. The strong dependence on the contact angle has already been discussed before. Another important factor is the surface tension σ entering with a cubic power. σ may be varied, for example, by impurities or particles removed from the surface, and this may explain, why at later times hydrophilic areas are also impacted. The pressure enters with a square power, but it contains many contributions, and here we would like to give merely an estimate: Taking the highest power used (51.3 W/cm^2), the acoustic pressure P_A amounts to 12.2 atm.[40] The vapor pressure P_V varies between room temperature and 340 K from 0.03 atm to 0.27 atm, which is comparatively little.[35] Figure 8a also shows that for typical pressures and surface energies the critical radius is on the order of 0.1 μm, scaling inverse linearly with pressure. Hence our finding that bubble nucleation predominates with higherθ and is accelerated by increased temperature (mainly via reduction of σ) and by ultrasonic power is in agreement with the model.

The question of defining a critical radius, contact angle, temperature, or pressure for caviation nucleation is similar to that of defining a rupture force for a ligand in a receptor in biology.[41] There the answer is that this rupture force depends on the logarithm of the pulling speed. Here the equivalent of pulling speed is given by the ultrasonic frequency determining the time of "pulling". However, there is an unknown frequency factor not allowing us to define, for example, a critical pressure threshold keeping all other parameters constant.

The model of an instantaneous thermally induced nucleation is not very probable in view of the high energy barriers involved. Instead we propose a slightly different model: The barrier in Figure 8 is a minimum value considering the time dependence, since it corresponds to the maximum pressure of acoustic

Scheme 3. SEM Images of the Patterned Al Plate after Ultrasonic Treatment: (c) at 30 min of Sonication, (e) at 40 min of Sonication; Inner Circular Area Is Hydrophilic; Outer Part Is Hydrophobi; Temperature of the Treatment is 340 K

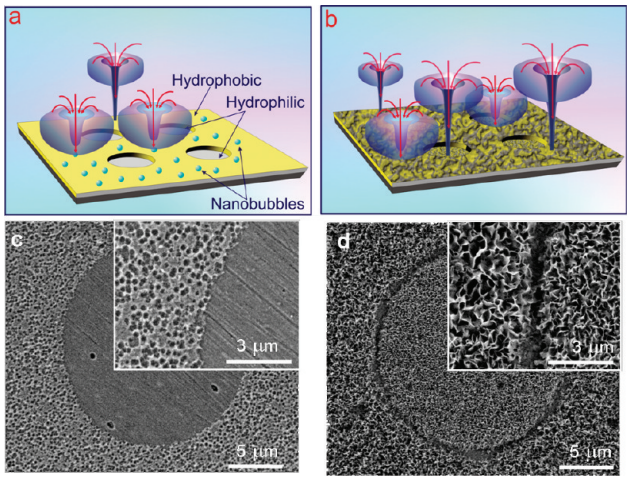

rarefaction. ΔE decreases and disappears during the pressure cycles upon compression, leading to a very small nanobubble that is stabilized by the Laplace pressure and again increased by the acoustic energy input. The latter increases stronger and faster if the opposing surface tension term in Figure 8 is reduced, e.g., by local heating, and thus accelerates nucleation. This model has to be verified in future studies varying the surface tension and ultrasonic frequency to get a quantitative and predictive way of surface modification.

We propose a possible mechanism of the selective nucleation process at the hydrophobic/hydrophilic microstructure (scheme 3). It is known that water may contain gas bubbles which can be the centres for nucleation in the bulk. Nano-sized bubbles are stabilized at the solid surface, preferably at the hydrophobic surface/water interface.[42,43] Likely, in our case, nano-sized bubbles as nucleation centres are present at the hydrophobic surface and attract reactive jets resulting from the collapse of the cavitation bubbles to the hydrophobic surface. The cavities formed under sonication on the hydrophobic surface become the new nucleation centres for further microjet impact. With increasing time of ultrasonic treatment the impacted area on the surface drastically increases and most of the pits merge. The drastic change in surface texture in this case may be due to the fact that initially formed pits present secondary nucleation sites.[44,45] Further cavitation occurs on both surfaces. In all cases, we find that gas nucleation at earlier stages of sonication occurs only on the hydrophobic surface, which according to our theoretical findings (eq 5) suggests that this is the energetically favorable location that reduces the nucleation barrier. A higher contact angle causes a lower energy barrier and thus cavitation occurs predominantly at the hydrophobic surface.

To verify that the presence of two different surfaces, hydrophobic and hydrophilic, plays a significant role for selective nucleation, we evaluated the situation for comparison when both surfaces are hydrophilic (Figure 8a). By oxidizing the pattern with plasma treatment we changed the chemical nature of the structured surface and the hydrophobic surface became hydrophilic (Plasma treatment removes the organic layer from hydrophobic parts (IR measurements) and slightly oxidizes uncovered Al areas). The IR spectrum shows that after plasma treatment the diffraction peaks of ODT and ODTA disappear. The measurement of the wettability shows a totally hydrophilic surface with CA smaller than 2°, which is less than the detection limit. Figure 8a shows a SEM image of the plasma-treated patterned Al after 10 min of sonication. It turned out that both surfaces are equally affected by sonication, where we observed a metal-foam structure (boehmite AlO(OH) and bayerite ($Al(OH)_3$). The CA after 10 min of ultrasonic irradiation increased up to 72°. Also the IRRA spectrum shows appearance of the hydroxyl group in the oxide film after 10 min of sonication (see Figure 2, bottom; plasma treatment). By comparing this result to the previous one (ultrasonic treatment of patterned Al with two different surfaces) the nucleation on both surfaces started 4 times faster. So, when both surfaces are hydrophilic the selectivity of the nucleation process disappears.

To prove that pits formed on the hydrophobic surface are caused by local cavitation at an earlier stage and not by increased surface temperature, we boiled a patterned Al (Figure 8b). By comparing Figure 8b and Figure 4c, it can be seen that the surface microstructures are different. After boiling treatment, the hydrophilic surface has a cellular structure with diameters ranging from 30 to 60 nm. The border of the print is mostly destroyed. Further boiling treatment significantly changes the morphology of the surface. A. N. Rieder et al. studied the effect of the boiling treatment on Al.[46] Evidently, under longer cavitation (more that 40 min), the morphology of the surface is similar to boiling treatment, and differences are predominantly revealed via the depth of the resulting nanostructures.

CONCLUSIONS

In conclusion, we demonstrated that selective control in the heterogeneous nucleation of gas bubbles near the solid/water interface can be achieved by varying surface energies, temperature and ultrasonic power. Different patterns with various millimeter-sized hydrophobic/hydrophilic areas have been investigated. By changing the surface energy (initial wettability of the patterned surface) it is possible to achieve a selective control of the heterogeneous nucleation of gas bubbles near the solid/water interface. At the earlier stage of sonication, the nanometer-sized corrugations appear only on the hydrophobic area, while the hydrophilic plane of the patterned Al is not affected by cavitation. Longer sonication periods affect both surfaces with different damaging level. These results confirm the expectation that higher contact angles cause a lower energy barrier, as a result cavitation dominates at hydrophobic surfaces. Experimental findings are in good agreement with those found by applying nucleation theory. This study offers a new direction in investigating ultrasound-induced nucleation processes at solid surfaces. Here, the main focus was given to heterogeneous nucleation of cavitation bubbles. Further dedicated and quantitative studies should thus pave a way making use of ultrasound to modify the geometry and chemistry of surfaces and films and to nucleate bubbles on microparticles of defined surface. This would be a major step for establishing this technology for broad use in materials science.

METHODS

Materials. The stamp material, sylgard-184 poly(dimethylsiloxane) (PDMS) and curing agent were obtained from Dow Corning GmbH, Germany. They were mixed in a 1:10 curing agent/prepolymer ratio. Stamp replication was performed in contact with a silicon master. Si-Masters with size 10×10 mm^2 were purchased from GeSiM mbH, Germany (Dresden). The aluminium alloy AA2024, was used as a model metal substrate. For all experiments, aluminium samples with the size of 10×20 mm^2 were polished and cleaned with methanol in an ultrasonic

bath for 15 min. A 100 nm thick aluminium layer was deposited by evaporation immediately prior to use.

Octadecanethiol (ODT, 96 % purity, Alfa Aesar), n-octadecylphosphonic acid (ODPA, Alfa Aesar), phosphoric acid, nitric acid, acetic acid, and ethanol, were used as received. Ink solution was freshly prepared before each set of experiments by dissolving ODT and ODPA in ethanol. Dissolution was supported by immersion in an ultrasound bath for about 10 min. All aqueous solutions were made using deionized Millipore Milli-Q water.

Microcontact Printing and Etching. A mixed solution of ODPA (10 mM in ethanol) and ODT (2 mM in ethanol) was filtered and dropped onto the PDMS stamp. The stamps (about 10×10 mm^2) were equilibrated for a 1 minute in the ink solution. The excess solution was removed under a steam of filtered N_2 gas. Stamping was performed manually by using tweezers for stamp handling and by taking advantage of the natural stamp-substrate adhesion. The contact time was 10 minutes. Printed aluminium samples were post-treated on a hot plate (70 °C) for 10 min.[47] The samples were etched at room temperature in open polyethylene containers using freshly prepared etching bath. The etchant (Aluminium Etchant Type "A") is a combination of phosphoric, acetic, and nitric acids and water in a ratio 16:1:1:2.[48]

Scanning Electron Microscopy (SEM). was performed with a Gemini Leo 1550 instrument at an operating voltage of 3 keV to study the morphology of Al. Samples were sputtered with gold.

Field-Emission Environmental Microscopy (ESEM). was performed with a high-resolution low vacuum FEI Quanda 600 FEG instrument at an operating voltage 30 kV with extended low-vacuum capabilities.

Atomic Force Microscopy (AFM). AFM analysis was performed on a Nanoscope III Multimode AFM (Digital Instruments Inc., USA) operating in tapping mode.

Contact Angle Measurements. The hydrophobicity of the fabricated prints on the aluminium plates was investigated by measuring water CAs with a contact angle meter (Software DSA 1, Krüss GmbH, Hamburg, Germany) at room temperature. 3μl of deionised Millipore Milli-Q water droplets were placed on the fabricated surfaces and apparent CAs were observed. CAs were measured at three different positions for each test sample.

IR Spectroscopy. Spectra were acquired with an IFS 66 Fourier transform (FT)-IR spectrometer from Bruker (Ettlingen, Germany) equipped with an external reflectance unit containing a Langmuir trough setup. The infrared beam was directed through the external port of the spectrometer and was subsequently reflected by three mirrors in a rigid mount before being focused on the sample surface. An AKRS-5 wire grid polarizer was placed into the optical path directly before the beam hit the sample surface. The reflected light was collected at the same angle as the angle of incidence. The light then followed an equivalent mirror path and was directed onto a narrow band mercury−cadmium-telluride detector, which was cooled by liquid nitrogen. The entire experimental setup was enclosed to reduce relative humidity fluctuations. For all measurements at 40 mN m^{-1}, p-polarized radiation was used at an angle of incidence of 70°. A total of 128 scans were acquired with a scanner velocity of 20 kHz at a resolution of 8 cm^{-1}.

Plasma Treatment. The patterned samples were oxidized by exposure of the surface to a Plasma Cleaner PDS-32 G-2 (medium 60 W) for a 5 min.

Software Image J is designed for the analysis of SEM imagery of structure. Image J is a widely used Open Source software in scientific communities employing Image Analysis and is released under the GPL license.[49]

AUTHOR INFORMATION

Corresponding Author

*Tel: +493315679235. Fax: +493315679202. E-mail: valentina.belova@mpikg.mpg.de.

ACKNOWLEDGMENT

The work was supported by the NanoFutur project of BMBF (German Ministry of Science and Education) and by the Gay-Lussac/Humboldt Award to H.M.. The authors thank Dr. Hartmann, Dr. T. Borodina, R. Pitschke, and A. Heilig for helping with SEM and AFM measurements. Special thanks to Dr. B. Porokhonski for helping with ImageJ Software. We thank the Mechanical center of the Max-Planck Institute of Colloids and Interfaces (Andreas Kretzchmar and Jan von Szada-Borryszkowski) for the pre-treatment the samples for all experiments.

REFERENCES

(1) Suslick, K. S.; Crum, L. A. *Sonochemistry and Sonoluminescence*; Wiley-Interscience: New York, 1997, Vol. 1.

(2) Didenko, Y. T.; McNamara, W. B.; Suslick, K. S. *J. Am. Chem. Soc.* **1999**, *121*, 5817–5818.

(3) Rae, J.; Aschokkumar, M.; Eulaerts, O; Reisse, C.; von Sonntag, J.; Grieser, F. *Ultrason. Sonochem.* **2005**, *12*, 325–329.

(4) Aschokkumar, M.; Hall, R.; Mulvaney, P; Grieser, F. *J. Phys. Chem. B* **1997**, *101*, 10845–10850.

(5) Suslick, K. S.; Flannigan, D. J. *Annu. Rev. Phys. Chem.* **2008**, *59*, 659–683.

(6) Lorimer, J. P.; Mason, T. J. *Chem. Soc. Rev.* **1987**, *16*, 239–274.

(7) Thomas, C. R.; Farny, C.H.; Coussios, C.C.; Roy, R. A.; Holt, R. G. *ARLO* **2005**, *6* (3), 182–187.

(8) Rayleigh, L. *Philos. Mag.* **1917**, *34*, 94–98.

(9) Philipp, A.; Lauterborn, W. *J. Fluid Mech.* **1998**, *361*, 75–116.

(10) Belova, V.; Möhwald, H.; Shchukin, D. G. *Langmuir* **2008**, *24* (6), 9747–9753.

(11) Belova, V.; Andreeva, D. V.; Möhwald, H.; Shchukin, D. G. *J. Phys. Chem. C* **2009**, *113*, 5381–5389.

(12) Kolesnikova, T. A.; Gorin, D. A.; Fernandes, P.; Kessel, S.; Khomutov, G. B.; Fery, A.; Shchukin, D. G.; Möhwald, H. *Adv. Funct. Mater.* **2010**, *20*, 1189–1195.

(13) Wei, Y.; Li, Y.; Zhang, N.; Shi, G.; Jin, L. *Ultrason. Sonochem.* **2010**, *17*, 17–20.

(14) Ross, N. A.; MacGregor, R. R.; Bartsch, R. A. *Tetrahedron* **2004**, *60*, 2035–2041.

(15) Ross, N. A.; Bartsch, R. A. *J. Org. Chem.* **2003**, *68* (2), 360–366.

(16) Ashokkumar, M.; Grieser, F. *Rev. Chem. Eng.* **1999**, *15*, 41–83.

(17) Andreeva, D. V.; Fix, D.; Möhwald, H.; et al. *Adv. Mater.* **2008**, *20*, 2789–2794.

(18) Fell, M.; Murphy, S. M. *J. Nucl. Mater.* **1990**, *172*, l–12.

(19) Heneghan, A. F.; Wilson, P. W.; Haymet, A. D. *Proc. Natl. Acad. Sci. U.S.A.* **2002**, *99* (15), 9631–9634.

(20) Jaschke, M.; Butt, H. J.; Gaub, H. E.; Manne, S. *Langmuir* **1997**, *13*, 1381–1384.

(21) Tuziuti, T.; Yasui, K.; Iida, Y.; Taoda, H.; Koda, S. *Ultrasonics* **2004**, *42*, 597–601.

(22) Marschall, H. B.; Morch, K. A.; Keller, A. P.; Kjeldsen, M. *Phys. Fluids* **2003**, *15*, 545–553.

(23) Melmed, A. J. *J. Appl. Phys.* **1966**, *37* (1), 275–279.

(24) Roldugin, V. I.; Tikhonov, N. A. *Phys. Chem.* **2002**, *383* (3), 362–365.

(25) Phan, H. T.; Caney, N.; Marty, P.; Colasson, S.; Gaville, J. *Mécanique* **2009**, *337*, 251–259.

(26) Nail, J. P., Jr.; Vachon, R. I.; Morehouse, J. *Trans. ASME. J. Heat Transfer* **1974**, *96*, 132–137.

(27) Bremond, N.; Arora, M.; Dammer, S. M.; Lohse, D. *Phys. Fluids* **2006**, *18*, 121505.

(28) Bremond, N.; Arora, M.; Ohl, C. D.; Lohse, D. *Phys. Rev. Lett.* **2006**, *96*, 224501.

(29) Harvey, E. N.; McElroy, W. D.; Whiteley, A. H. *J. Appl. Phys.* **1947**, *18* (2), 162–172.

(30) Borkent, B. M.; Gekle, S.; Prosperetti, A.; Lohse, D. *Phys. Fluids* **2009**, *21*, 9.
(31) Steitz, R.; Gutberlet, T.; Hauss, T.; Klösgen, B.; Krastev, R.; Schemmel, S.; Simonsen, A. S.; Findenegg, G. H. *Langmuir* **2003**, *107*, 1316–1320.
(32) James, W. G.; Attard, T.; P. *Phys. Rev. Lett.* **2001**, *87*, 176104.
(33) Belova, V.; Gorin, D. A.; Shchukin, D. G.; Möhwald, H. *Angew. Chem. Int. Ed.* **2010**, *49*, 7129–7133.
(34) Blander, M.; Katz, J. L. *AlChE* **1975**, *21*, 833–848.
(35) *CRC Handbook of Chemistry and Physics*; CRC Press: Boca Raton, FL, 2004; p 47.
(36) Mason, T. *Chem. Soc. Rev.* **1997**, *26*, 444.
(37) Raman, A.; Dubey, M.; Gouzman, I.; Gawalt, E. S. *Langmuir* **2006**, *22*, 6469–6472.
(38) Wolska, E.; Szajda, W. *J. Appl. Spectrosc.* **1983**, *38*, 137–140.
(39) Rider, A. N.; Arnott, D. R. *Int. J. Adhes.* **2000**, *20*, 209–220.
(40) Mason, T. J. *Chemistry with Ultrasound*; Elsevier: London, 1990, Vol. 28, p 190.
(41) Merkel, R.; et al. *Nature* **1999**, *397*, 50–53.
(42) Ishida, N.; Inoue, T.; Miyahara, M.; Higashitani, K. *Langmuir* **2000**, *16*, 6377–6380.
(43) Yang, S.; Dammer, S. M.; Bremond, N.; Zandvliet, H. J. W.; Kooij, E. S.; Lohse, D. *Langmuir* **2007**, *23*, 7072–7077.
(44) Khurana, A. K.; Chen, H.; Wall, C. G. *Chem. Eng. Corn.* **1998**, *165*, 199–215.
(45) Nail, J. P. J.; Vachon, R. I.; Morehouse, J. *Trans. ASME. J. Heat Transfer* **1974**, *96*, 132.
(46) Rider, A. N.; Arnott, D. R. *Int. J. Adhes.* **2000**, *20*, 209.
(47) Goetting, L. B.; Deng, T.; Whitesides, G. M. *Langmuir* **1999**, *15* (4), 1182–1191.
(48) *Materials Safety Data Sheet for Aluminium Etchant Type A*; Transience Co. Inc.: Danvers, MA.
(49) Free Software Foundation GNU General Public License. Web site: http://www.gnu.org/licenses/licenses.html#GPL